Decreased ATP synthase activity is linked to altered spatiotemporal organisation of ATP Synthase in a cellular cardiomyocyte senescent model

Silke Morris[1*], Frank Schmelter[1], Isidora Molina-Riquelme[2], Stefan Peischard[3], Paul Disse[3], Guiscard Seebohm[3], Verónica Eisner[2], Karin Busch[1*]

[1]Institute of Integrative Cell Biology and Physiology, Schlossplatz 5, Faculty of Biology, University of Muenster, 48149 Muenster, North-Rhine-Westphalia (Germany)
[2]School of Biological Sciences, Pontificia Universidad Católica de Chile, Avda. Libertador Bernardo O'Higgins 340 Santiago de Chile (Chile)
[3]Institute for Genetics of Heart Diseases (IfGH), Department of Cardiovascular Medicine, University Hospital Münster, D-48149 Münster, North-Rhine-Westphalia (Germany)

[*]Corresponding authors:

Prof. Dr. Karin Busch
Institute of Integrative Cell Biology and Physiology
Faculty of Biology
University of Münster
Schlossplatz 5
48149 Muenster, Germany
Phone: +49-(0) 251-83-21560
Mail: buschkar@uni-muenster.de

Dr. Silke Morris
Institute of Integrative Cell Biology and Physiology
Faculty of Biology
University of Münster
Schlossplatz 5
48149 Muenster, Germany
Phone: +49-(0) 251-83-21563
Mail: silke.morris@uni-muenster.de

Abstract

Heart disease is the leading cause of death in the elderly population and the heart is a highly energy-consuming tissue. The high energy requirement is reflected in the abundance of mitochondria in cardiomyocytes and the cristae dense architecture of the organelles. The ATP synthase is well known for its involvement in ATP synthesis, but it also plays an important structural role. This is reflected in its spatiotemporal organisation, making single molecule localisation microscopy in living cells a valuable tool to study ATP synthase under different conditions. In the present study, we studied the effects of cellular senescence on the ATP Synthase in cardiomyocytes. We used human induced pluripotent stem cell derived cardiomyocytes as a model system and induced senescence with low doses of doxorubicin. We observed reduced function of the ATP Synthase while membrane potential was increased, indicating a malfunction of the proton sink. These impairments could however not be related to changes in neither expression nor dimerization levels of the complex. Using single-molecule tracking of ATP synthase, we observed stronger confinement of the enzyme in the cristae.

This suggests that the altered spatiotemporal organisation of ATP synthase is linked with impaired ATP production in senescent cardiomyocytes.

1. Introduction

Cardiovascular diseases (CVDs) are tightly coupled to aging and the leading cause of death in the elderly population, accounting for almost 40 % of all age-related ailments [1]. The process of aging and the onset of age-related cardiovascular diseases are strongly linked to reduced energy metabolism and thereby decreased mitochondrial function.

Mitochondria are responsible for a multitude of tasks ranging from signal transduction [2] to induction of apoptosis [3]. But first and foremost, they are known as the powerhouses of the cell. Energy transformation in the form of ATP synthesis through oxidative phosphorylation (OXPHOS) is carried out by the OXPHOS complexes (Complex I-IV) and ATP synthase (Complex V) located in the inner mitochondrial membrane (IMM). The IMM is folded into cristae, which increases the surface area but also poses a physical barrier, the cristae junctions, to the highly dynamic proteins diffusing within the membrane [4]. Cristae themselves are highly dynamic and have recently been shown to undergo complex apparent fusion and fission processes [5]. In fact, it has been suggested that cristae architecture plays a significant role in organisation and function of the OXPHOS complexes [6].

Mitochondrial function is reflected in the cristae architecture [7]. This implies that cells with high energy demand, such as cardiomyocytes and other muscle cells, contain a large number of mitochondria with a comparatively high cristae density. In a recent study, we established a model of human induced pluripotent stem cell derived cardiomyocytes (hiPSC-CM) in which we induced senescence via mild treatment with doxorubicin [8]. We then compared the said model with primary rat neonatal ventricular cardiomyocytes (NVCM), in which we induced senescence using the same method. Our investigations found that both models display a compromised IMM ultrastructure upon induction of senescence. This included reduced cristae density, as well as altered cristae morphology. We witnessed a higher number of truncated cristae and partially cristae-depleted mitochondria. Conducting experiments with photoactivatable GFP tagged to Complex I, the NADH-ubiquinone oxido-reductase, we observed shorter fusion completion time of the IMM in senescent CM, implying that the dynamic organisation of OXPHOS complexes is also affected in both models. As we recently showed, the spatiotemporal organisation of the ATP synthase is tightly coupled to its function [9]. Besides its role as ATP generator of the cell, the ATP synthase serves a structural function. Dimers and oligomers of the complex at the cristae tips contribute to the stabilisation of the cristae structure [10], and display reduced mobility compared to monomers [11]. Due to its forward, respectively reverse proton pumping activity, ATP synthase determines the pH at cristae rims [11]. Under OXPHOS conditions, the proton motive force generated by Complexes I, III and IV of the electron transport chain (ETC) is used for ATP synthesis. Under unfavourable conditions for OXPHOS, ATP synthase ensures the stability of the electrochemical membrane potential ($\Delta\psi_M$) across the IMM by working in reverse mode as an ATP hydrolysing enzyme, or ATPase. Thus, mitochondria still uphold their membrane potential under hypoxic or glycolytic conditions, when ATP production by OXPHOS is not possible [12, 13] to guarantee the transport of positively charged proteins and metal ions into the mitochondrial matrix [14, 15]. In a previous work, we showed that ATPase has a higher mobility than ATP synthase, reflecting once again how protein dynamics are coupled to their function [9].

In the following study, we aimed to elucidate the molecular mechanisms behind the bioenergetic impairment seen in senescent hearts. Our experimental approach is built upon the results of our previous work, where we observed ultrastructural changes in combination with reduced mitochondrial function and increased ROS production under senescent conditions. We investigated how ATP production by OXPHOS is affected in senescent cardiomyocytes and examined $\Delta\psi_M$ as well as ETC complex composition and activity as potential causes. In addition, we studied ATP synthase function and organisation in depth. We evaluated mitochondrial ATP production, oligomeric states of the ATP synthase and performed experiments on its spatiotemporal organisation in control and senescent CM. To induce senescence, we used mild doxorubicin treatment as previously characterised [16]. Our findings indicate that senescent cells exhibit reduced ATP synthesis but an increased membrane potential. We did not detect changes in ATP synthase dimerization or oligomerisation, suggesting that ATP synthase was not responsible for ultrastructure alterations. Single molecule tracking data revealed a decreased diffusion coefficient of ATP synthase, which we assign to the observed alteration of the cristae architecture. This let us conclude that the cristae ultrastructure is critical for optimal spatiotemporal organisation and function of ATP synthase.

2. Experimental Procedures

2.1 Cell Culture and Differentiation of hiPSC

All cells were routinely cultured in a humidified atmosphere of 5% CO_2 and 37°C. Senday Foreskin 1 (SFS.1) cells were cultured in FTDA Medium [17] on plates coated with Matrigel (Corning, #354263) with daily medium exchange. Cells were passaged when they reached 100% confluency under presence of Rock-inhibitor Y-27632 (R&D Systems, #1254/10). Differentiation into cardiomyocytes (hiPSC-CM) was carried out according to Peischard *et al.* ([18]. Briefly, cells were seeded at high density of 500 000 cells per well of a 24-well plate on day 0 of differentiation in differentiation medium [19]. Concentrations of BMP-4 were batch dependant and were determined in a first test differentiation. Medium was exchanged daily with fresh TS-ASC medium [19] for 7-10 days until autonomous beating was observed. To ensure differentiation into cardiomyocytes, the WNT pathway was inhibited by adding C59 on days 2 and 3 of differentiation. After differentiation, cells were frozen in liquid nitrogen. For experiments, hiPSC-CMs were thawed and seeded out on plastic coated with 0.2 % gelatine (Sigma Aldrich, #G1393) or glass coated with 0.2 % gelatine and FBS (PAN Biotech, #P30-3031) and cultured for at least 2 weeks prior to experiments.

2.2 Cardiac Myocyte Isolation and Culture

Cardiomyocytes were isolated from the hearts of neonatal Sprague–Dawley rats as described previously [31]. Rats were bred in the Bioterio of the Pontificia Universidad Católica de Chile. All studies followed the Guide for the Care and Use of Laboratory Animals published by the US National Institutes of Health (NIH Publication No. 85-23, revised 1996) and were approved by Institutional Ethics Review Committee. Briefly, ventricles were dissected, pooled, and myocytes dissociated in a solution of collagenase (Worthington #LS004176) and pancreatin (Sigma Aldrich #8049-47-6). After enzymatic dissociation, the cells were selectively enriched for cardiac myocytes (NVCMs) by being plated in F-10 Ham medium (Gibco #11550-043) supplemented with 10% (v/v) horse serum (Gibco #16050-114), 5% (v/v) fetal bovine serum (Gibco #16000-044), penicillin and streptomycin (100 units/ml; Thermo Scientific #15140122). The NVCMs were plated on top of 2% (w/v) gelatine-coated glass coverslips. Finally, the cells were kept at 37°C in a humid atmosphere of 5% CO_2. 5-bromo-2-deoxyuridine (Sigma Aldrich #59-14-3) was added to prevent the proliferation of remaining fibroblasts.

2.3 Induction of Senescence

Senescence was induced by treatment with 50 nM doxorubicin (Doxo, Sigma Aldrich, #D1515) for 96 h according to Morris *et al.* [8].

2.4 Generation of a Stable Cell Line

For generation of an SFS.1 cell line stably expressing the subunit gamma (SUγ) of the ATP synthase fused to the HaLo tag (SUγ-HaLo), a triple vector system was used. The main vector was a well-established stem-cell Tet-On transfection vector, KAO717-pPB-hCMV1-IRES-Venus (A) [20-22], in which we inserted the gene sequence for SUγ-HaLo [9, 23]. We did this by amplifying the sequence for SUγ-HaLo from the original vector using primers with overhanging ends containing restriction sites for XhoI and NotI (highlighted in bold), which allowed cloning of the sequence into KAO717-pPB-hCMV1-IRES-Venus (B) via the same restriction sites.

Fwd: 5'- **CTCGAG**ATGTTCTCTCGCGCGGGTGTCG -3'

Rev: 5'- **GCGGCCGC** ACCGGAAATCTCCAGAGTAGAC -3'

Expression of SUγ-HaLo was hence controlled by the CMV_{min} promotor. The Venus marker that was encoded on the transfection vector allowed for easy detection of positive clones and was controlled by an IRES2 sequence. The second vector was KA0637-pPgCAG-rtTAM2-IN. This vector contained a G418 resistance gene for selection of positive clones, as well as the rTA transactivator sequence that allows doxycycline-inducible expression of SUγ-HaLo. The last vector of the trio was PB200PA-1 (C). This encoded the PiggyBac transposase that enabled stable insertion into the genome of transfected hiPS cells.

We transfected SFS.1 cells with Lipofectamine 3000 (Thermo Fisher Scientific, #L3000-001) according to the manufacturer's instructions using the three plasmids at a ratio of A:B:C = 15:3:1. Medium was changed after 8 hours. The optimal concentration of G418 was previously determined by generation of a kill curve. We started selection with 50 µg ml^{-1} G418 (Sigma Aldrich, #A1720) 24 h after transfection, then increased this to 150 µg ml^{-1} after 48 h and finally to 200 µg ml^{-1} after 120 h. Selection was considered complete when no more cells were viable in the non-transfected control, which was 12 days post-transfection. Cells were then seeded in a dilution series onto a 96-well plate, which led to monoclonal cultures in some wells. Selection pressure was reduced to 20 µg ml^{-1} for another 5 days before G418 was not added to the culture medium anymore. Monoclonal cultures were expanded and expression was induced with 0.25 µg ml^{-1} doxycycline. Heterogenous expression of Venus (green) and SUγ-HaLo (labelled with HTL-TMR) was confirmed via confocal microscopy. Clones that did not express the two constructs were discarded. Subsequently, a test differentiation into cardiomyocytes was carried out as described above.

Before experiments, expression of SUγ-HaLo was induced by adding 0.25 µg ml^{-1} doxycycline for 96 h.

2.5 Quantitative PCR

Total RNA was extracted from differentiated hiPSC-CMs using the Monarch Total RNA Miniprep Kit (NEB #T2010) and equal amounts of RNA per sample were transcribed into cDNA using the GoScript™ Reverse Transcription Kit (Promega #A5000). Quantitative PCR (qPCR) was carried out on a StepOnePlus™ Real Time PCR System (Thermo Scientific) using the PowerUP™ SYBR™ Green Master Mix (Applied Biosystems #A25741), between 60 and 80 ng of cDNA and 0.1 nM of each forward and reverse primer per reaction. The PCR program consisted of an initial denaturation step at 95°C for 10 min followed by 40 cycles of 95°C for 15 s and 60°C for 60 s. A melting curve was generated after the run (60°C to 95°C at 0.8°C increase per minute). GAPDH served as endogenous control. Primers were synthesised by Eurofins Genomics.

TARGET	FORWARD SEQUENCE 5' – 3'	REVERSE SEQUENCE 5' – 3
GAPDH	CTG GTA AAG TGG ATA TTG TTG CCA T	TGG AAT CAT ATT GGA ACA TGT AAA CC
NDUFA9	AGC TTC ATC ATG CCC TCA TGC C	TCT CGC GTC CCA TTC CAG AAA C
NDUFV1	TGT GTG AGA CGG TGC TGA TGG A	CGA TGG CTT TCA CGA TGT CCG T
SDHA	GCA AAA TCA TGC TGC CGT GTT C	ATC CGC ACC TTG TAG TCT TCC C
UQCC3	ATG CTA AAG GAG ATG CCA CTG C	GCC AAC CAT CCA GTT CTT CCT C
COX8A	AAG ATC CAT TCG TTG CCG C	TAG GTC TCC AGG TGT GAC AG
ATP5F1A	CCA AAC CAG GGC TAT GAA GCA G	CAC CCG CAT AGA TAA CAG CCA C
ATP5F1B	GAA GAC AAG TTG ACC GTG TCC C	TCA CGA TGA ATG CTC TTC AGC C

2.6 Western Blotting

Cells were lysed in RIPA Buffer (Thermo Scientific, #89901) with added protease inhibitor (Thermo Scientific, #78430). Protein quantification in lysates was performed by modified Bradford assay (Roti Nanoquant, Roth, #K880). Equal protein amounts were supplemented with 4x SDS-PAGE sample buffer and subsequently loaded on a 10% (w/v) polyacrylamide gel. After electrophoresis, gels were transferred onto a PVDF membrane. Membranes were blocked with 10% milk and immunoblotting was performed. Primary antibody was the OXPHOS rodent WB antibody cocktail (abcam, #ab110413), secondary antibody the goat anti-mouse secondary antibody (Jackson ImmunoResearch, #115-035-068). Visualisation of bands was enabled by chemiluminescence (SuperSignalTM West PICO PLUS, Thermo Scientific, #34580) and membranes were stained with Coomassie blue for signal normalisation.

2.7 Mitochondria Isolation and Blue Native Gel Electrophoresis

Blue Native gel electrophoresis (BN-PAGE) was conducted according to Wittig *et al.* [24]. SUγ-HaLo SFS.1 and neonatal rat ventricular cardiomyocytes (NVCM) were grown in a T75 culture flask to confluency. After harvesting, the cell pellet was resuspended in ice cold mitochondrial isolation buffer consisting of 300 mM sucrose, 5 mM TES, and 200 µM ethyleneglycoltetraacetic acid (EGTA), pH 7.2. Cells were then lysed mechanically by slowly passing the cell suspension six times through a cell homogeniser (Isobiotec) using a 6 µm clearance tungsten carbide ball and glass syringes (Hamilton). The obtained lysate was subjected to centrifugation at 4°C, 800 x *g* for 10 min 3 times to remove nuclei and cell debris. The mitochondria containing supernatant was subsequently centrifuged at 4°C, 9000 x *g* for 15 min. The resulting pellet contained mitochondria and was resuspended in mitochondrial isolation buffer. Protein concentration was quantified by Bradford assay (ROTI Nanoquant, Roth, #K880.3). 50 µg protein was subjected to another round of centrifugation at 4°C,

9000 x *g* for 10 min and the resulting pellet was resuspended in blue native sample buffer [24] supplied with 4% digitonin (Sigma Aldrich, #D5628). Samples were separated on a 3 – 12% polyacrylamide gradient gel (Serva, #43250) alongside a molecular weight marker (NativeMark, Thermo Fisher Scientific, #LC0725). After electrophoresis, the gel was transferred to a PVDF membrane and western blotting was performed using an anti-Halo primary antibody (Promega, #G9211) and a goat anti-mouse secondary antibody (Jackson ImmunoResearch, #115-035-068). For visualisation of Complex V, anti-ATPB (subunit β of the ATP synthase, abcam, cat# ab170947) was used as a primary antibody and goat anti-rabbit (Jackson ImmunoResearch, cat# 111-035-045) as secondary antibody. Bands were visualised by chemiluminescence (Super Signal West PICO PLUS, Thermo Fisher Scientific, #34580).

2.8 Seahorse Extracellular Flux Analysis

Seahorse Extracellular Flux Analysis allows the measurement of the oxygen consumption rate (OCR) and the extracellular acidification rate (ECAR) as well as the Proton Efflux Rate (PER) which is derived from the ECAR, while injecting the samples with different reagents, such as inhibitors or substrates of complexes of the electron transport chain. We used the Seahorse Extracellular Flux Analyzer (Agilent Technologies) to perform an ATP rate assay and a complex activity assay.

Differentiated hiPSC-CMs were grown on gelatine coated 96-well Seahorse plates for at least two weeks before the experiment. On the day prior to the experiment, the Seahorse XF extracellular flux assay sensor cartridge was hydrated with calibrant solution (Agilent Technologies, #100840-000) and incubated at 37 °C overnight.

The ATP rate assay was performed according to the manufacturer's instructions (Agilent Technologies, #103592-100). Briefly, cells were washed with PBS and medium exchanged for Seahorse XF Base Medium Minimal DMEM (Agilent Technologies, #102353) supplied with 10 mM glucose, 1 mM pyruvate, and 2 mM glutamine. The inhibitors were loaded into the ports of the cartridge to obtain the following final concentrations: Oligomycin, 1.5 µM (port A) and Rotenone/Antimycin A, 0.5 µM (port B). The ATP production rate was then determined from the following equations:

glycoATP Production Rate [pmol ATP min^{-1}] = glycoPER [pmol H^+ min^{-1}]

glycoPER [pmol H^+ min^{-1}] = PER [pmol H^+ min^{-1}] – mitoPER [pmol H^+ min^{-1}]

PER [pmol H^+ min^{-1}] = ECAR [mpH min^{-1}] × Buffer Factor [mmol H^+ $L^{-1}pH^{-1}$] × Volume [µL] × K_{Vol}

mitoPER [pmol H^+ min^{-1}] = mitoOCR [pmol O_2 min^{-1}] × CCF [pmol H^+ $pmol^{-1}$ O_2]

mitoOCR [pmol O_2 min^{-1}] = OCR_{basal} [pmol O_2 min^{-1}] – $OCR_{Rot/AA}$ [pmol O_2 min^{-1}]

OCR_{ATP} [pmol O_2 min^{-1}] = OCR_{basal} [pmol O_2 min^{-1}] – OCR_{Oligo} [pmol O_2 min^{-1}]

mitoATP Production Rate [pmol ATP min^{-1}] = OCR_{ATP} [pmol O_2 min^{-1}] × 2 [pmol O_2 $pmol^{-1}$ O_2] × P/O [pmol ATP $pmol^{-1}$ O]

The complex activity assay was carried out to analyse the activity of individual respiratory chain complexes. This assay took place in the presence of digitonin to allow entry of membrane impermeable compounds. Before the assay, cells were washed with PBS and medium was exchanged for MAS++ buffer. This consisted of 220 mM Mannitol, 70 mM Sucrose, 10 mM KH_2PO_4, 2 mM HEPES, 1 mM EGTA, 5 mM $MgCl_2$, 10 mM glutamate, 10 mM malate, 0.5 µM FCCP, and 0.00006 % digitonin, pH was adjusted to 7.4 with HCl or KOH. Inhibitors and substrates were the following: Rotenone (CI inhibitor),

0.5 mM (port A), Succinate and glyceraldehyde 3-phosphate (CII substrates), 10 mM (port B), Antimycin A (CIII inhibitor), 0.5 µM (port C), Ascorbate, 10 mM and tetramethyl-p-phenylenediamine (TMPD), 100 µM (CIV substrates, port D). In addition, port D was loaded with 0.2 µg ml^{-1} Hoechst 33342 (Thermo Scientific, #H3570) to allow for determination of the cell count via de Cytation 5 image reader and normalisation of the OCR to the cell number.

2.9 Live Cell Imaging

Fluorescence microscopy was carried out on a confocal laser scanning microscope (Leica TCS SP8 SMD) equipped with a 63× water objective (N.A. 1.2) and a tuneable white light laser. HyD's with GaASP photocathodes were used as detectors. Measurements were performed in a humidified chamber at 37 °C and 5% CO_2. Membrane potential was determined by staining the cells with 7 nM TMRE (Thermo Scientific, #T669) and 100 nM MitoTracker™ Green (MTG, Thermo Scientific, #M7514) for 30 min and subsequent imaging. Image analysis was carried out in ImageJ by measuring the fluorescence intensity of single cells in both channels. The TMRE signal was then normalised pixelwise to the MTG signal. In a separate experiment, loss of mitochondrial membrane potential was induced by addition of 10 µM FCCP and time lapses were recorded at an acquisition rate of 1 frame per 3 seconds. Resting membrane potential was then calculated as $\Delta = I_{basal} - I_{CCCP}$ using absolute intensity values.

ATP levels were determined by staining with 10 µM of the fluorogenic dye BioTracker ATP-Red (Sigma Aldrich, #SCT045). Before measurements, cells were stained with MTG (100 nM for 30 min). Image analysis was carried out in ImageJ by measuring the fluorescence intensity of single cells in both channels and normalising the ATP-Red intensity to the MTG intensity.

2.10 Immunofluorescence Staining

For immunofluorescence staining, cells were cultured on cover glasses, washing with PBS was carried out after each step. Prior to staining, cells were fixed with 4% PFA for 20 min at room temperature. Residual PFA activity was quenched by incubation in 0.1 M Glycine for 10 min. Cover glasses were then incubated in 0.1% Triton X-100 in PBS for 4 min to allow permeabilization of the cells and subsequently blocked in 5% normal goat serum in PBS for 30 min. Staining was then carried out by incubating the cover glasses with the primary antibody anti-α-actinin (Sigma Aldrich #A7811) diluted 1:400 in blocking buffer for 60 min and with the secondary antibody pAb to RbIgG, tagged with Alexa Fluor 555 (abcam, #150078) diluted 1:400 for 60 min. glasses were then mounted onto microscope slides and left to dry overnight before imaging.

2.11 Tracking and Localisation Microscopy

Tracking and Localisation Microscopy (TALM) was carried out as previously described [25]. Differentiated hiPSC-CM were treated with doxorubicin as described or left untreated. 96 h prior to the experiment, expression of SUγ-HaLo was induced using 0.25 µg ml^{-1} doxycycline. One day before the experiment, cells were transferred onto ibidi glass bottom dishes (ibidi, #81156). For imaging, cells were stained with 1 nM Halo Tag Ligand (HTL) tagged with Janelia Fluor 646 (HTL-JF646, Promega, #GA1110) for 30 min at 37°C. Subsequently, cells were washed three times with PBS and phenolred-free medium was added to the cells for imaging. Cells were imaged at room temperature on an Olympus TIRF 4 Line system equipped with a 100x oil immersion TIRF objective (N.A. 1.49) and a diode pumped solid-state laser (excitation 640 nm, 140 mW). Imaging was carried out with a highly inclined and laminated optical sheet (HILO) [26], which was achieved by decreasing the illumination angle just below the critical angle for total internal reflection (TIR). 5000 frames were recorded at a frame rate

of 58 Hz (17 ms per frame) with a back-illuminated EMCCD camera (Hamamatsu CMOS Model C14440-20UP, pixel size 65 nm).

The labelling density was low enough to allow the identification of single molecules. To confirm mitochondrial localisation of the signals, a cumulative projection of all frames was generated. Localisation and generation of single molecule trajectories were carried out based on algorithms described by Sergé *et al.* [27]. These were implemented in a custom made Matlab code, SLIMfast (provided by C.P. Richter, University of Osnabrück). Briefly, the point spread function (PSF) was experimentally determined by fitting a 2D Gaussian function over the signals. Based on this, single molecules were localised in each frame with an error probability of 10^{-7}. Localisations were then connected between frames to form trajectories. Only trajectories were included in the analysis that consisted of at least 5 steps (85 ms) and the search radius was limited to be between 13 and 130 nm (0.2 and 2 pixels).

2.12 Statistical Analysis

For statistical analysis, data was tested for normal distribution. In case of normal distribution, statistical significance was determined by One-Way-ANOVA followed by Tukey's Range Test. For non-parametric testing, Kruskal-Wallis ANOVA was used.

3. Results

3.1 ATP Production is Reduced in Senescent hiPSC-CM

In our previous study we could show reduced mitochondrial function in senescent hiPSC-CM. Oxygen consumption rate (OCR) measurements showed that basal and maximal respiration were lower [8]. We asked, whether this affects ATP production rates and ATP levels. Therefore, we visualised mitochondrial ATP levels with the fluorescent probe ATP-Red [28] and determined ATP synthesis rates via OCR and determination of the extracellular acidification rate (ECAR) in the absence and presence of oligomycin, antimycin A and rotenone. We could show that ATP levels decrease significantly upon induction of senescence. ATP levels were determined with the dye ATP-Red1™ and normalised to the MitoTracker™Green (MTG) signal. We found a reduction of mitochondrial ATP levels from 2.06 a.u. (Median ± 1.68, SD) to 1.63 a.u. (Median ± 1.58, SD, $p<0.001$) (Figure 1A). To validate these results, we performed measurements of the oxygen consumption rate (OCR) as well as proton efflux rate (PER) via extracellular flux analysis (Seahorse/Agilent) from which ATP production levels can be derived. We saw a decrease of total ATP production from 678 pmol min^{-1} (Median ± 172, SD) to 586 pmol min^{-1} (Median ± 168, SD, $p<0.01$), OXPHOS-related ATP production (MitoATP) decreased from 390 pmol min^{-1} (Median ± 114, SD, $p=0.03$) to 368 pmol min^{-1} (Median ± 125, SD), while glycolysis-related ATP production decreased from 281 pmol min^{-1} (Median ± 63, SD) to 241 pmol min^{-1} (Median ± 50, SD, $p<0.001$) (Figure 1B). Due to technical issues, it was not possible to normalise this data to the cell number, however, equal distribution of cells was visually confirmed before running the experiment. Interestingly, when determining the percentage of OXPHOS and glycolysis-related ATP production (Figure 1C), we saw a slight decrease of OXPHOS-related ATP production from 56.75 % (Median ± 3.33, SD) to 55.58 % (Median ± 2.13, SD, $p=0.03$), but glycolysis-related ATP production slightly increased from 43.25 % (Median ± 3.33, SD) to 44.42 % (Median ± 2.13, SD, $p=0.03$). This indicates that ATP production is reduced overall in doxorubicin-induced senescence and that the cells are somewhat more dependent on glycolysis to cover their energy requirements, as the ATP synthesis activity of OXPHOS is apparently impaired.

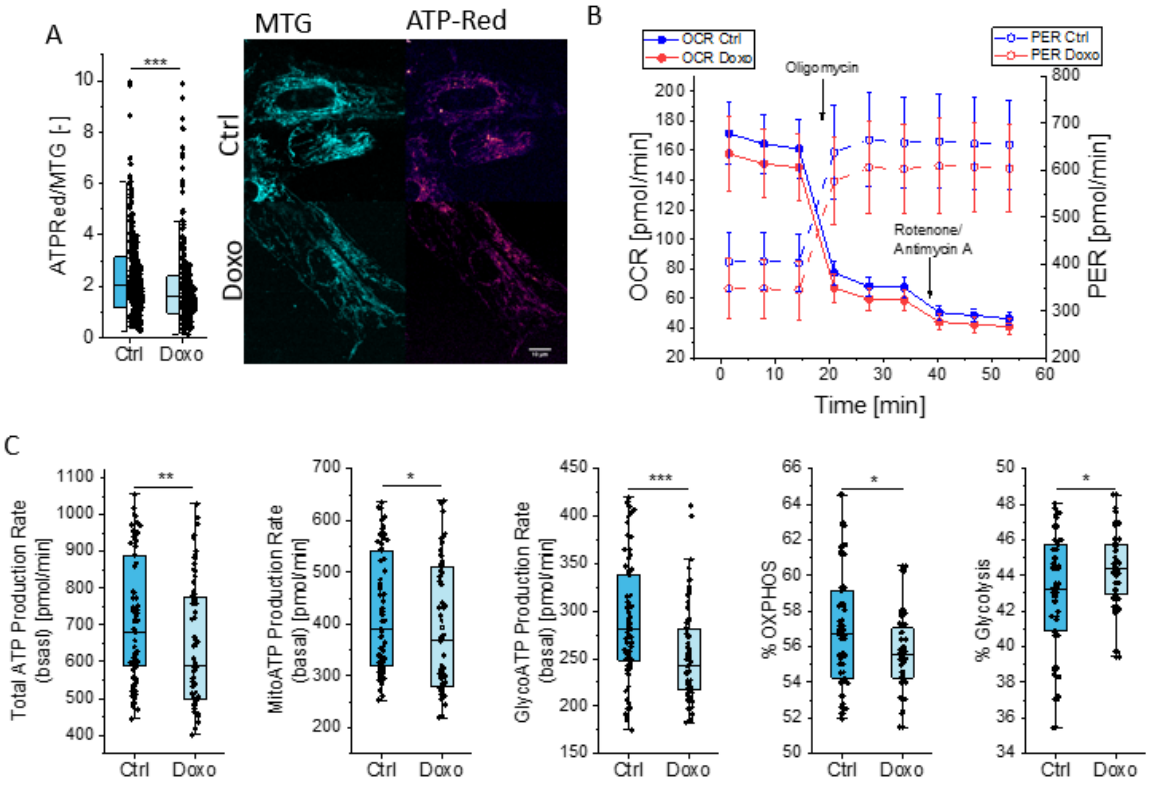

*Figure 1: Senescent cardiomyocytes exhibit reduced ATP production. hiPSC-CM were treated with 50 nM doxorubicin for 4 days (Doxo) or left untreated (Ctrl). (A) Cells were stained with ATP-Red and MitoTracker™Green (MTG) and fluorescence intensity was measured in both channels. The ratio of ATP-Red and MTG intensity was plotted and showed a decrease in doxorubicin treated cells. (B) Representative time course of ATP Rate Assay carried out via Seahorse extracellular flux analysis. OCR as well as PER were determined in the basal state, after addition of Oligomycin, and after addition of Rotenone/Antimycin A. Doxorubicin treated cells show lower respiration and proton efflux rates in all conditions. (C) From (B) total, mitochondrial, and glycolytic ATP production rate could be determined, as well as percentage of OXPHOS- and glycolysis-derived ATP production rate. Statistical significance was determined by Kruskal-Wallis ANOVA because of non-normal distribution of the data. The vertical lines in the box plots represent the median values, the error bars denote the standard deviation (SD), the boxes represent the 25th to 75th percentile. Significance: * $p \leq 0.05$, ** $p \leq 0.01$, *** $p \leq 0.001$. (A) N = 3 biological replicates, 468 cells (ctrl), 483 cells (doxo). Single points indicate measurements of single cells. Scale bar: 10 µm (C) N = 3 biological replicates, 77 (ctrl) and 69 (doxo) wells per condition were included in the analysis. MitoATP Production Rate: p = 0.034, %OXPHOS: p = 0.026, %Glycolysis: p = 0.026.*

3.2 Senescent hiPSC-CM show elevated $\Delta\Psi_m$ but not ETC complex activity

To correlate ATP levels to the electrochemical gradient, we determined the mitochondrial membrane potential in control and senescent hiPSC-CMs via staining with the membrane potential sensitive dye Tetramethylrhodamine ethyl ester perchlorate (TMRE) and MitoTracker™Green (MTG) for signal normalisation. We observed a significantly increased membrane potential from 1.13 a.u. (Median ± 0.61, SD) to 1.28 a.u. (Median ± 0.60, SD, *p<0.001*) (Figure 2A). To confirm this result, we determined the fluorescence intensity of the TMRE signal before and after addition of 10 µM of the uncoupler FCCP, results are plotted as $\Delta\Delta\psi_M$ (Figure S1). Senescent cells displayed a similar response to the uncoupler as control cells.

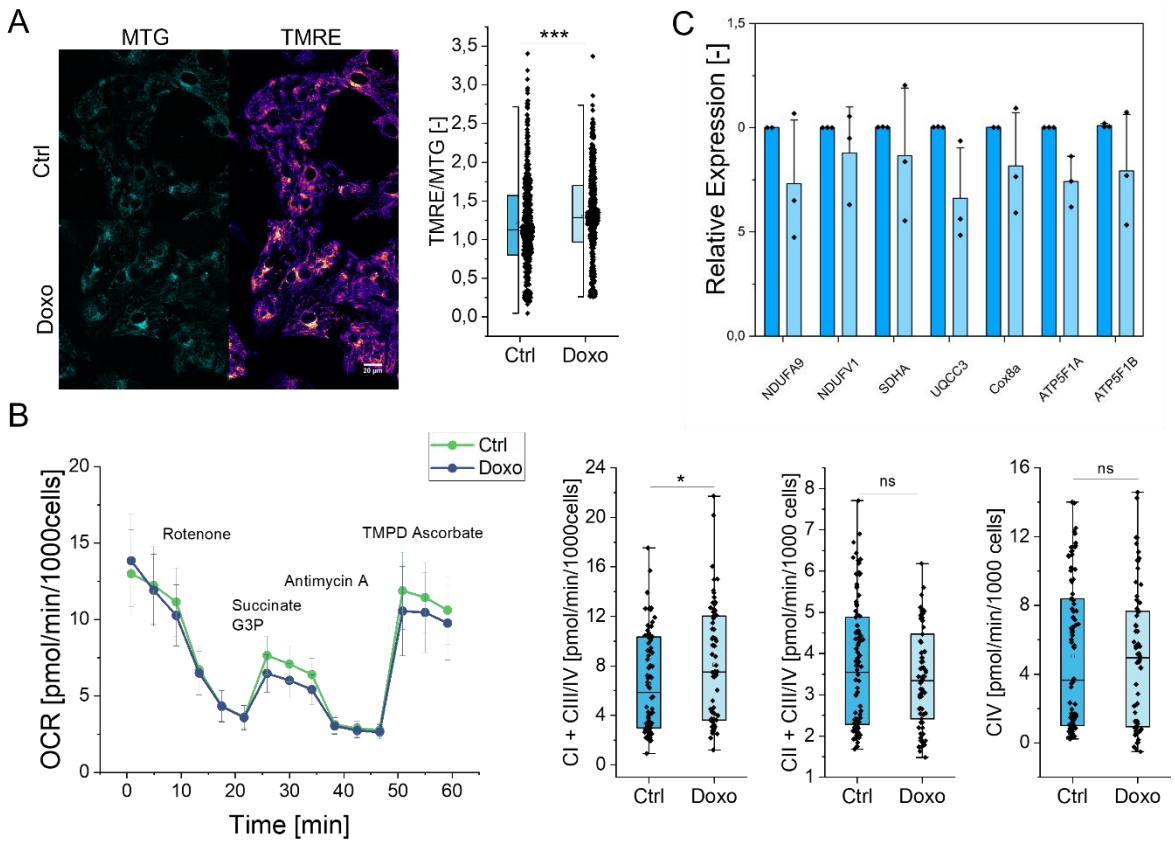

Figure 2: OXPHOS profiling of senescent cardiomyocytes. *hiPSC-CM were treated with 50 nM doxorubicin for 4 days (Doxo) or left untreated (Ctrl). (A) Membrane potential was measured by staining with TMRE and MTG. TMRE staining is shown as hot colour coded. Increased fluorescence intensity is particularly apparent in the perinuclear area. Fluorescence intensity was measured in both channels and the ratio was determined, which was increased in doxorubicin treated cells. N = 4 biological replicates, 469 cells (ctrl), 493 cells (doxo). Single points indicate measurements of single cells. (B) Complex activity assay was performed via Seahorse extracellular flux analysis. OCR was recorded after challenging the cells with Rotenone (CI inhibitor), Succinate/G3P (CII substrate), Antimycin A (CIII inhibitor), and TMPD/Ascorbate (CIV substrate). From the time course, the complex activities can be calculated. Statistical significance was determined by Kruskal-Wallis ANOVA in case of non-normal distribution of the data, one-way ANOVA was used in case of normal distribution. The vertical lines in the box plots represent the median values, the error bars denote the standard deviation (SD), the boxes represent the 25th to 75th percentile. Significance: * $p \leq 0.05$, ** $p \leq 0.01$, *** $p \leq 0.001$. (A) N = 3 biological replicates, 90 (ctrl) and 66 (doxo) wells per condition were included in the analysis. CI + III/IV activity: $p = 0.028$. (C) Relative expression of different complex subunits was determined via qPCR, GAPDH acted as housekeeping gene. Scale bar: 10 µm (A).*

To determine whether the apparently increased membrane potential is due to an increased activity of the ETC complexes, we performed a Complex Activity Assay. The Complex Activity Assay is performed in permeabilised cells and features the injection of inhibitors and substrates of the ETC complexes, allowing the extraction of the OCR related to CI + CIII/CIV, CII + CIII/CIV, as well as CIV alone. An exemplary time course of the experiment is shown in Figure 2B. From this graph, data for the CI + CIII/CIV activity can be extracted by subtracting the OCR after CI inhibition with Rotenone from the basal OCR. Similarly, CII + CIII/CIV activity is extracted by subtracting the OCR after CIII inhibition with Antimycin A from the OCR after addition of the CII substrates succinate and glyceraldehyde-3-phosphate. Finally, CIV activity can be determined by adding the artificial electron donor Tetramethylphenylendiamin (TMPD) that can transfer electrons directly to cytochrome c, which transfers them to CIV and subtracting this value from the CI and CIII inhibited respiration. Interestingly, we witnessed that the activity of CI, was slightly increased in these experiments when comparing the mean values of all three biological replicates. It increased from 5.86 pmol min^{-1} 1000 cells^{-1} (Median ± 3.96, SD) to 7.52 pmol min^{-1} 1000 cells^{-1} (Median ± 4.77, SD, *p=0.03*). The activity of CII remained

unaltered with Ctrl 3.55 pmol min^{-1} 1000 $cells^{-1}$ (Median ± 1.55, SD) and Doxo 3.34 pmol min^{-1} 1000 $cells^{-1}$ (Median ± 1.19, SD). CIV activity was also found unaltered with Ctrl 3.64 pmol min^{-1} 1000 $cells^{-1}$ (Median ± 4.29, SD) and Doxo 4.94 pmol min^{-1} 1000 $cells^{-1}$ (Median ± 4.05, SD). To check, whether protein expression levels of OXPHOS complexes were changed, we conducted a quantitative RT-PCR. We did not find altered expression levels of subunits of the ETC complexes using GAPDH as a housekeeping gene which did not show altered C_T values after doxorubicin treatment (Figure 2C). Also, protein levels of subunits NDUFA9 and NDUFV1 (CI), SDHA (CII), UQCC3 (CIII), Cox8a (CIV) were unaltered in senescent cells (Figure S2). Since the complexes and activity of the ETC were not conspicuously changed, we conclude that the increase in $\Delta\Psi_m$ has another reason. In accordance with reduced mitochondrial ATP levels, we suggest that mitochondrial ATP synthesis was impaired.

3.3 Expression and Oligomer Assembly of ATP Synthase is Unaltered in Senescent CM

We checked whether the protein level of ATP synthase is changed in senescent CM. Immunostaining of subunit α (ATP5A) showed no difference in the protein level (Figure 3A). ATP synthase is found in several forms: subcomplexes, monomers, dimers and oligomers. To test whether reduced OXPHOS activity was related to changes in the supramolecular organisation of ATP synthase, we performed Blue Native Gel-electrophoresis (BN-PAGE) and immunostaining (Figure 3B).

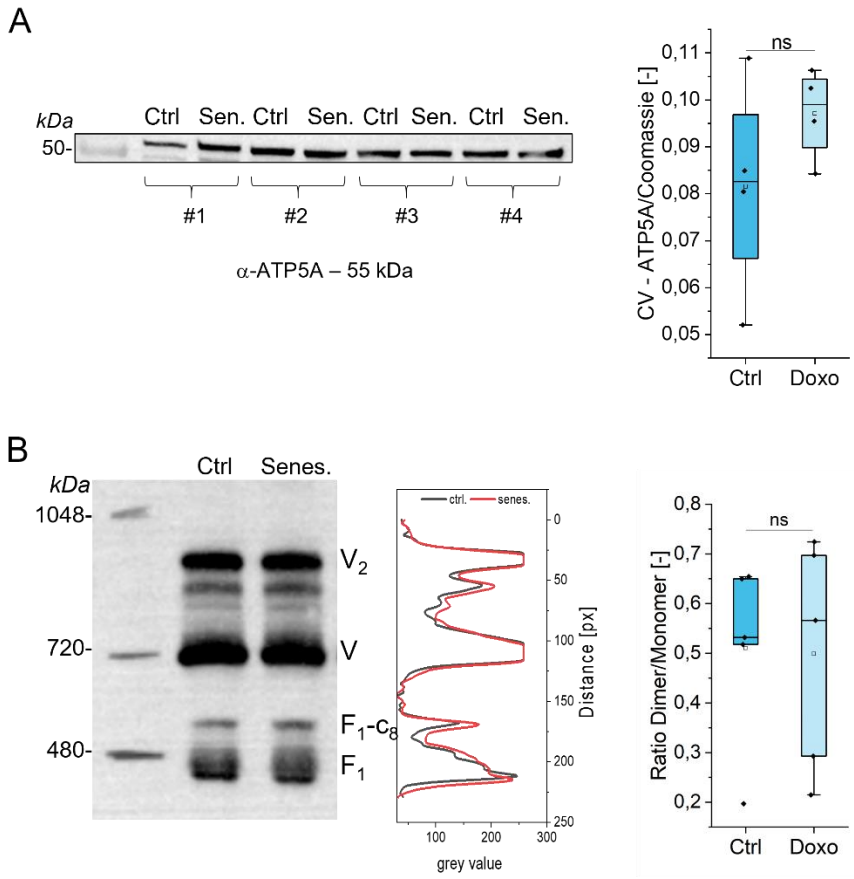

Figure 3: Expression and supramolecular organisation of ATP synthase is not altered in senescent CM. Senescent hiPSC-CM and NVCM were generated by treatment with 50 nM doxorubicin for 4 days (Doxo)). (A) Immunostaining of ATP synthase subunit α after protein separation by SDS-PAGE. Protein levels were normalised to total protein load as determined by staining with Coomassie Blue. (B) Blue native PAGE of isolated mitochondria from Ctrl and doxorubicin treated NVCM, shows no difference in ATP Synthase monomer/dimer formation using an antibody for subunit β. The representative gel shows the dimer

(V_2), monomer (V), as well as F_1 subunit bound to ring of c-subunits (F_1-c_8) and F_1. Statistical significance was determined by Kruskal-Wallis ANOVA because of non-normal distribution of the data. The vertical lines in the box blots represent the median values, the square symbols the mean values, the error bars denote the standard deviation (SD), the boxes represent the 25th to 75th percentile. Single points indicate mean values of technical replicates. (A) N = 4 biological replicates and N = 3 technical replicates. (B) N = 4 biological replicates, N = 3 technical replicates.

We isolated mitochondria from neonatal rat cardiomyocytes that had been treated with doxorubicin to induce senescence and performed blue native gel electrophoresis (BN-PAGE). In the past, we had observed similar behaviours of this cell type to our hiPSC derived model [8]. We chose this for mitochondrial isolation and subsequent BN-PAGE due to the ability to harvest enough cell material, which would be highly impracticable for hiPSC-CMs. We found no differences in the relative amount of ATP Synthase subcomplexes, monomers and dimers between control and doxorubicin treated cells (Figure 3B). Apparently, the supramolecular organisation of ATP synthase is not the key for its decreased function. Also, the compromised ultrastructure during doxorubicin-induced senescence is not related to alterations in ATP dimer formation.

3.4 Spatiotemporal Dynamics of ATP Synthase is Reduced during Senescence

As the supramolecular organisation of ATP synthase was obviously not the reason for the reduced ATP synthase activity, we asked whether the kinetic coupling between ETC and ATP synthase might be altered in senescent cells [29]. Under basal conditions, ETC complexes and super-complexes are found in the cristae sheet, while dimeric and oligomeric ATP synthase accumulates at cristae rims [10]. This physical separation results in a lateral pH gradient between proton pumps [30]. We hypothesise that optimal function is related to the specific localisation of ATP synthase complexes within the IMM sub-compartments cristae tips, cristae sheets and inner boundary membrane. In order to determine the sub-compartmental localisation, Tracking and Localisation Microscopy (TALM) of single molecules was used. Therefore, we generated a stable hiPSC line expressing SUγ fused to the self-labelling Halo-Tag which can be fluorescence-labelled via the HaloTag-Ligand [31]. We used a triple-vector system described earlier to successfully stably transfect hiPS cells [20] and generated monoclonal cultures. The correct assembly of the tagged SUγ with ATP synthase was tested by immunostaining of a BN-PAGE-blot of isolated mitochondria from undifferentiated WT and SUγ-Halo hiPSC. We found the monomeric form of Complex V (V), with an additional faint band also visible at the size of the dimer (V_2) (Figure S3). Staining with an α-Halo antibody confirmed the presence of the labelled subunit at the expected sizes of monomeric and dimeric Complex V. In addition, we observed bands for the F_1 subunit, which consists of subunits α, β, γ, δ and ε, as well as the F_1-c_8 subcomplex, which is the F_1 subunit with a bound ring of c-subunits [32, 33]. We confirmed correct differentiation into cardiomyocytes by visual observation of uniform beating of the cell layer (see Supp Video 1) and by immunofluorescence staining of the sarcomere protein and cardiomyocyte marker α-actinin (Figure S3). Lastly, we confirmed correct localisation of the Halo-tagged SUγ within mitochondria by co-localisation with TMRE in undifferentiated cells and found a Pearson's coefficient of 0.558 (Mean ± 0.086, SD) (Figure S3).

We used this hiPSC stable cell line to perform single molecule localisation and tracking experiments in living cardiomyocytes. The principle of this method is based on the ability to circumvent the diffraction limit [34] by only labelling a subpopulation of molecules of interest. Keeping the labelling density to a minimum prevents the overlapping of neighbouring signals, thus enabling the detection of single molecule signals. Imaging the labelled cells with a high frame rate allows the generation of trajectories from each tagged molecule as long as it is visible in the focal plane. From these trajectories on the

other hand, parameters on the molecule mobility can be extracted. Signals were fitted by a 2D-Gaussian considering the experimentally determined point spread function. The signal from three single molecules ATP Synthase is exemplarily shown in Figure 4A together with a representation of the localisation of a single molecule based on its fitted 2D-Gaussian. We recorded videos with 1000 to 5000 frames, the z-projection of all localisations in an exemplary stack is shown in Figure 4C, while the resulting trajectories are shown in Figure 4D. The z-projection as well as the accumulated trajectories form structures that clearly resemble rod-like mitochondria (aspect ratio >1). This was confirmed by recording one image at high exposure time (100 ms) in which no single molecules but mitochondrial structures are clearly seen. The trajectory map was merged with this image (Figure 4B). The trajectories are located within the mitochondria and most trajectories are arranged perpendicular to the mitochondrial axis, illustrating the ATP Synthase's movement along the cristae (Figure 4E). Slight discrepancies are due to the movement of mitochondria within the time of imaging, since the high exposure image was recorded before the recording of single molecules at high frame rate. An additional image after recording was not possible, since mitochondrial structures were not visible anymore due to extensive photobleaching. We repeated the experiment in 3 technical replicates and obtained a total of 9220 trajectories for control conditions and 4576 for doxorubicin treated cells.

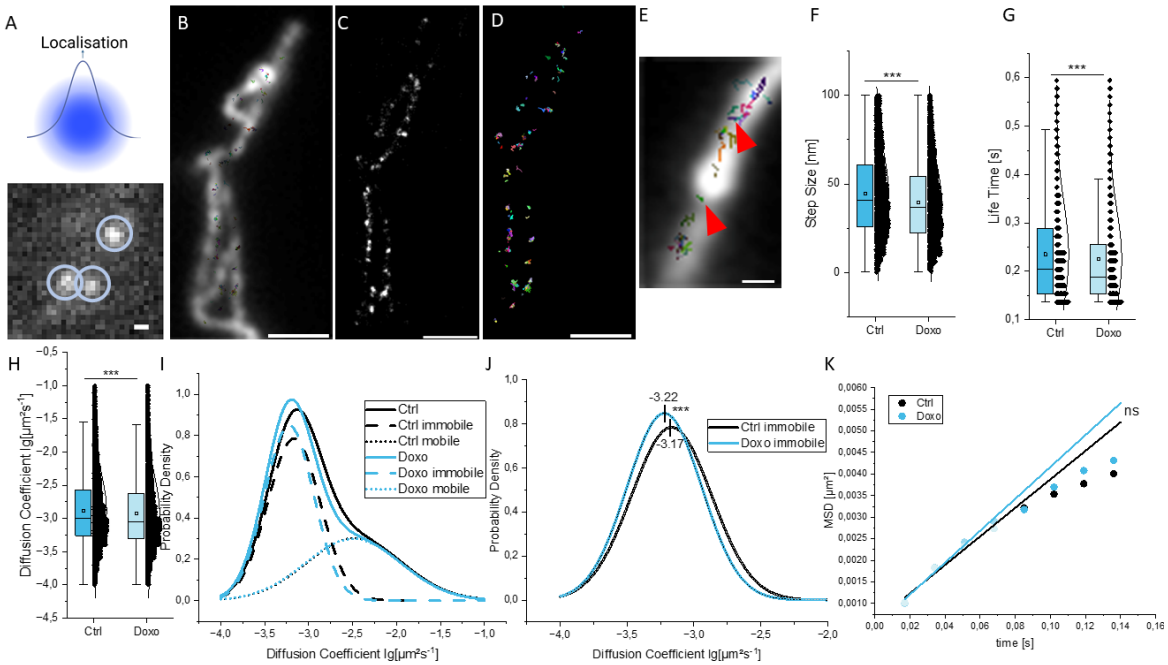

*Figure 4: Single molecule localisation and tracking of ATP synthase shows decreased mobility of ATP synthase. Stably expressing SUγ-Halo hiPSC-CM were treated with 50 nM doxorubicin for 4 days (Doxo) or left untreated (Ctrl) (A) Exemplary single molecules as well as graphical illustration of the point spread function and localisation (B) Trajectories overlayed on an image with high exposure time (mitochondria instead of single molecules visible) (C) Cumulative image of localisations from 5000 frames (D) Trajectories from 5000 frames (E) Orthogonal trajectories to the mitochondrial axis indicated by red arrows (F) Step size is decreased in doxorubicin treated cells (G) Life time is decreased in doxorubicin treated cells (H) Diffusion coefficient is decreased in doxorubicin treated cells (I) Probability density distribution of diffusion coefficients of single molecules (solid line). Fitted for two populations, a mobile (dashed line) and an immobile population (dotted line) (J) Probability density distribution of mobile populations fitted with an amplified Gaussian fit (K) Mean Square Displacement over time modelled with a linear fit over the first 0.07 s. Statistical significance was determined by Kruskal-Wallis ANOVA because of non-normal distribution of the data. The vertical lines in the box blots represent the median values, the error bars denote the standard deviation (SD), the boxes represent the 25th to 75th percentile. Significance: * $p \leq 0.05$, ** $p \leq 0.01$, *** $p \leq 0.001$. (A) Scale bar: 500 nm, (B-D) Scale bar: 1 µm (E) Scale bar: 250 µm (F) N = 3 biological replicates, 7710 trajectories (ctrl), 2690 trajectories (doxo). Single points indicate measurements of single trajectories. (G-H) N = 3 biological replicates, 9220 trajectories (ctrl), 4576 trajectories (doxo). Single points indicate measurements of single trajectories.*

The step size (Figure 4F) relates to the distance each molecule travels between frames in nm. This is reduced in doxorubicin treated cells from 44.4 nm (Median ± 34.6 nm, SD) to 39.2 nm (Median ± 39.0 nm, SD, *p<0.001*). The life time of the fluorophore attached to the ATP synthase, which is related to its redox state amongst others, (Figure 4G) was reduced from 0.20 s (Median ± 0.11 s, SD) to 0.19 s (Median ± 0.10 s, SD, *p<0.001*). The diffusion coefficient *D*, related to the velocity of single molecules, is displayed as logarithmic values for ease of presentation. The total diffusion coefficient for all molecules decreased from log(-2.99) $\mu m^2 s^{-1}$ (Median ± log (0.54) $\mu m^2 s^{-1}$, SD) to log(-3.05) $\mu m^2 s^{-1}$ (Median ± log(0.54) $\mu m^2 s^{-1}$, SD, *p<0.001*) in senescent cells. This is shown in Figure 4H, whereas Figure 4I depicts the probability density of the total population (solid lines). This distribution can be fitted for 2 subpopulations, one representing the population of mobile molecules (dotted lines) and one that of immobile molecules (dashed lines). The mobile populations of both control and doxorubicin treated cells virtually overlap and show no difference. However, the immobile population of ATP synthase in senescent cells is clearly shifted to the left, suggesting a decrease in mobility. This is more clearly depicted in Figure 4J, where we only show the probability density distribution of the immobile population. Modelling the peak with an amplified Gaussian fit (dashed lines) and comparison of the two models showed that the peak maxima were indeed shifted from log(-3.17) $\mu m^2 s^{-1}$ to log(-3.22) $\mu m^2 s^{-1}$ (*p<0.001*). We were curious to see whether there was also an effect on the mean square displacement (MSD) of the molecules. This is defined as the deviation of a molecule's localisation from its original position over time. The function of the MSD is hereby restricted by spatial limitations of the cristae and has therefore a confined character depicted as a saturated exponential function. In the short range, however, diffusion can be assumed to be random and therefore follows a linear function. We modelled the short-range diffusion between 0.00 s and 0.07 s with a linear fit, as shown in Figure 4K, and compared the slopes of these functions, but found no statistically significant difference, indicating that the reduced diffusion coefficient of the doxorubicin treated group had no effect on the MSD of these molecules. In sum, we found a shorter mean step size and an overall reduced mobility of ATP synthase in senescent cells. This is expected, when the cristae are truncated, respectively shorter, as observed before [16].

4. Discussion

Senescence has negative effects on the mitochondrial performance in cardiomyocytes. We have recently established a senescence model of induced pluripotent stem cell derived cardiomyocytes and could show that this behaves remarkably similar to a previously established cell model of neonatal rat cardiomyocytes, in which senescence was induced by treatment with doxorubicin [35, 36]. Both models exhibit clear markers of cellular senescence, and we observed compromised mitochondrial function as well as ultrastructure, with an increase in truncated and curved cristae [8].

With the present study, we aimed to further elucidate the molecular mechanisms behind this phenotype. Mitochondrial dysfunction and reduced respiratory capacity are well-known hallmarks of aging in different cell models and cardiomyocytes [37, 38]. Accordingly, we observed reduced mitochondrial ATP synthesis in our senescent hiPSC-CM model. Senescent cardiomyocytes tend to shift to increased glucose usage as their preferred fuel und thus exhibit a higher rate of glycolysis. This has been related to age-related hyperglycemia, insulin resistance and type II diabetes, which are together with aging, principal risk factors for the development of cardiovascular diseases [39]. Interestingly, our model also shows a higher proportion of glycolysis compared to oxidative phosphorylation, even though there is decreased ATP production via both pathways, albeit the mitochondrial membrane potential was increased. An increased membrane potential was also observed in naturally aged mouse

hearts and was related to increased ROS producing activity of CI [40]. This is also reflected in our data. We observed increased membrane potential measured by TMRE staining and noted a slight increase in CI activity. Hence, our data supports Lima Rosa's observations and our previously reported increase in ROS production [8].

Apparently, ATP synthase could not utilise the increased $\Delta\Psi_m$ for ATP synthesis. Alternatively, ATP synthase itself could contribute to the generation of $\Delta\Psi_m$ by working in the reverse mode and hydrolysing ATP, possible due to cells being cultured in a high-glucose medium. To dissect these possible functions, we determined the spatiotemporal organisation of ATP synthase, since we recently observed that ATP hydrolysis was linked to dissociation of dimeric and oligomeric ATP synthase [11]. On the molecular level, we found no changes in the fractions of monomeric, dimeric and oligomeric ATP synthase in senescent cells, though this analysis was done with doxorubicin-treated neonatal ventricular cardiomyocytes from mice (NVCMs). Also, levels of ATP synthase were not changed. This is similar to observations in a model of naturally aged mice with no changes in expression levels of ATP synthase subunits [41].

Although we detected no obvious differences in the expression and molecular organisation of ATP synthase, the intramitochondrial localisation of ATP synthase might be changed. This could influence the coupling with the ETC and optimal usage of the proton motive force. To determine the spatiotemporal organisation of ATP Synthase in the inner mitochondrial membrane, we conducted tracking and localisation microscopy (TALM). First, we found that the trajectories had a shorter lifetime, which can be related to the elevated ROS levels in the doxorubicin treated group [8]. ROS can quench fluorescence and has therefore an influence on properties such as intensity and lifetime. Importantly, we observed significant changes in ATP synthase spatiotemporal dynamics with regards to the step size and diffusion coefficient. Both factors were significantly reduced and analysing the diffusion coefficient further, we saw that this concerned exclusively the mobile population. The immobile population, which is thought to be comprised of dimers and higher order oligomers of the ATP Synthase [42], was not affected by doxorubicin treatment. Under consideration of the altered ultrastructure of the IMM in senescent CM with increased number of truncated cristae [8], this may directly restrict movement, reduce maximal step size and thus decrease the diffusion of ATP synthase. This effect is independent of the molecular organisation of ATP synthase. Since ETC and ATP synthase are kinetically coupled via the proton motive force (PMF), and as recently shown by our group, the PMF has a local junction resulting in a lateral gradient between the proton source (ETC complexes) and sink (ATP synthase) [30], we conclude that the truncation of the cristae changes the distance between source and sink and thus affects the proton distribution and $\Delta\Psi_m$. Ultrastructural changes with reduced distance between ETC and ATP synthase might provide unfavourable conditions for ATP synthesis resulting in a decreased efficiency of ATP production in the senescent cardiomyocytes. This would provide an explanation for the increase in heart failure at increased age.

As we kept our cells under high glucose, glycolysis was able to compensate for the reduced ATP synthesis. This means that changes in the efficiency with which ATP is produced become even more important when OXPHOS is the preferred source of ATP, as it is in the heart. Another important player in both, cristae ultrastructure and molecule mobility, is the lipid composition of the membrane. Cardiolipin is a phospholipid that can be found exclusively in the IMM. It differs from other membrane phospholipids by its characteristic conical structure, which is thought to aid the bending of the IMM into cristae [43, 44]. The cardiolipin acyl chain composition is very heterogenous and can differ

between different cell types but has also been shown to be affected by aging. A study in rat heart tissue has shown that cardiolipins from aged animals contain more and longer unsaturated acyl chains. An effect that was not observed in other phospholipids [45]. In addition to its structural role, Cardiolipin has been shown to be associated with the complexes and supercomplexes of the OXPHOS machinery and absence leads to destabilisation of supercomplexes as well as reduced enzymatic function [46, 47]. It is conceivable, but has not been tested to date, whether it also affects ATP synthase mobility and function, in which case this would explain the differences we observed. Cardiolipin can furthermore act as a potential drug target for the prophylaxis and treatment of age-associated heart failure. Last but not least, ATP synthase functionality should be investigated more specifically. This could be arranged for example by determination of the P:O ratio, the number of phosphorylations of ADP to ATP in relation to reduction of oxygen.

5. Bibliography

1. Fajemiroye, J.O., et al., *Aging-Induced Biological Changes and Cardiovascular Diseases.* BioMed Research International, 2018. **2018**: p. 1-14.
2. Picard, M. and O.S. Shirihai, *Mitochondrial signal transduction.* Cell Metabolism, 2022. **34**(11): p. 1620-1653.
3. Wang, C. and R.J. Youle, *The Role of Mitochondria in Apoptosis.* Annual Review of Genetics, 2009. **43**(1): p. 95-118.
4. Wilkens, V., W. Kohl, and K. Busch, *Restricted diffusion of OXPHOS complexes in dynamic mitochondria delays their exchange between cristae and engenders a transitory mosaic distribution.* J Cell Sci, 2013. **126**(Pt 1): p. 103-16.
5. Kondadi, A.K., et al., *Cristae undergo continuous cycles of membrane remodelling in a MICOS-dependent manner.* EMBO reports, 2020. **21**(3).
6. Stephan, T., et al., *Live-cell STED nanoscopy of mitochondrial cristae.* Scientific Reports, 2019. **9**(1).
7. Cogliati, S., J.A. Enriquez, and L. Scorrano, *Mitochondrial Cristae: Where Beauty Meets Functionality.* Trends in Biochemical Sciences, 2016. **41**(3): p. 261-273.
8. Morris, S., et al., *Inner mitochondrial membrane structure and fusion dynamics are altered in senescent human iPSC-derived and primary rat cardiomyocytes.* Biochimica et Biophysica Acta (BBA) - Bioenergetics, 2023. **1864**(2): p. 148949.
9. Salewskij, K., et al., *The spatio-temporal organization of mitochondrial F1FO ATP synthase in cristae depends on its activity mode.* Biochimica et Biophysica Acta (BBA) - Bioenergetics, 2020. **1861**(1): p. 148091.
10. Davies, K.M., et al., *Structure of the yeast F1Fo-ATP synthase dimer andits role in shaping the mitochondrial cristae.* Proc. Natl. Acad. Sci., 2012. **109**: p. 13602-13607.
11. Weissert, V., et al., *Inhibition of the mitochondrial ATPase function by IF1 changes the spatiotemporal organization of ATP synthase.* Biochimica et Biophysica Acta (BBA) - Bioenergetics, 2021. **1862**(1): p. 148322.
12. Di Lisa, F., et al., *Mitochondrial membrane potential in single living adult rat cardiac myocytes exposed to anoxia or metabolic inhibition.* Journal of Physiology, 1995. **486**(1): p. 1-13.
13. Rieger, B., et al., *Mitochondrial F(1) F(O) ATP synthase determines the local proton motive force at cristae rims.* EMBO Rep, 2021. **22**(12): p. e52727.
14. Garlid, K.D. and P. Paucek, *Mitochondrial potassium transport: the K+ cycle.* Biochimica et Biophysica Acta (BBA) - Bioenergetics, 2003. **1606**(1-3): p. 23-41.
15. Maguire, M.E., *Magnesium Transporters: Properties, Regulation and Structure.* Frontiers in Bioscience, 2006. **11**(3): p. 3149-3163.
16. Morris, S., et al., *Inner mitochondrial membrane structure and fusion dynamics are altered in senescent human iPSC-derived and primary rat cardiomyocytes.* Biochim Biophys Acta Bioenerg, 2023. **1864**(2): p. 148949.
17. Frank, S., et al., *Small Molecule-Assisted, Line-Independent Maintenance of Human Pluripotent Stem Cells in Defined Conditions.* PLoS ONE, 2012. **7**(7): p. e41958.
18. Peischard, S., et al., *From iPSC towards cardiac tissue—a road under construction.* Pflügers Archiv - European Journal of Physiology, 2017. **469**(10): p. 1233-1243.

19. Rao, J., et al., *Stepwise Clearance of Repressive Roadblocks Drives Cardiac Induction in Human ESCs.* Cell Stem Cell, 2016. **18**(3): p. 341-353.
20. Peischard, S., et al., *The first versatile human iPSC-based model of ectopic virus induction allows new insights in RNA-virus disease.* Scientific Reports, 2020. **10**(1).
21. Estarás, C., et al., *YAP repression of the WNT3 gene controls hESC differentiation along the cardiac mesoderm lineage.* Genes & Development, 2017. **31**(22): p. 2250-2263.
22. Quaranta, R., et al., *Revised roles of ISL1 in a hES cell-based model of human heart chamber specification.* eLife, 2018. **16:7**.
23. Appelhans, T., et al., *Nanoscale Organization of Mitochondrial Microcompartments Revealed by Combining Tracking and Localization Microscopy.* Nano Letters, 2012. **12**(2): p. 610-616.
24. Wittig, I., H.-P. Braun, and H. Schägger, *Blue native PAGE.* Nature Protocols, 2006. **1**(1): p. 418-428.
25. Appelhans, T. and K. Busch, *Single Molecule Tracking and Localization of Mitochondrial Protein Complexes in Live Cells.* 2017. **1567**: p. 273-291.
26. Tokunaga, M., N. Imamoto, and K. Skata-Sogawa, *Highly inclined thin illumination enables clear single-molecule imaging in cells.* Nature Methods, 2008. **5**: p. 159-161.
27. Sergé, A., et al., *Dynamic multiple-target tracing to probe spatiotemporal cartography of cell membranes.* Nature Methods, 2008. **5**(8): p. 687-694.
28. Wang, L., et al., *A Multisite-Binding Switchable Fluorescent Probe for Monitoring Mitochondrial ATP Level Fluctuation in Live Cells.* Angewandte Chemie International Edition, 2015. **55**(5): p. 1773-1776.
29. Toth, A., et al., *Kinetic coupling of the respiratory chain with ATP synthase, but not proton gradients, drives ATP production in cristae membranes.* Proceedings of the National Academy of Sciences, 2020. **117**(5): p. 2412-2421.
30. Rieger, B., W. Junge, and K.B. Busch, *Lateral pH gradient between OXPHOS complex IV and F0F1 ATP-synthase in folded mitochondrial membranes.* Nature Communications, 2014. **5**(1).
31. Appelhans, T., et al., *Nanoscale organization of mitochondrial microcompartments revealed by combining tracking and localization microscopy.* Nano Lett, 2012. **12**(2): p. 610-6.
32. Wittig, I., et al., *Supercomplexes and subcomplexes of mitochondrial oxidative phosphorylation.* Biochimica et Biophysica Acta (BBA) - Bioenergetics, 2006. **1757**(9-10): p. 1066-1072.
33. He, J., et al., *Assembly of the peripheral stalk of ATP synthase in human mitochondria.* Proc. Natl. Acad. Sci., 2020. **117**(47): p. 29602-29608.
34. Abdullah, C.S., et al., *Doxorubicin-induced cardiomyopathy associated with inhibition of autophagic degradation process and defects in mitochondrial respiration.* Scientific Reports, 2019. **9**(1).
35. Spallarossa, P., et al., *Doxorubicin induces senescence or apoptosis in rat neonatal cardiomyocytes by regulating the expression levels of the telomere binding factors 1 and 2.* American Journal of Physiology - Heart and Circulatory Physiology, 2009. **297**(6): p. H1965-H2269.
36. Maejima, Y., et al., *Induction of premature senescence in cardiomyocytes by doxorubicin as a novel mechanism of myocardial damage.* Aging Cell, 2007. **7**(2): p. 125-136.
37. Martini, H. and J.F. Passos, *Cellular senescence: all roads lead to mitochondria.* The FEBS Journal, 2022. **290**(5): p. 1186-1202.
38. Lee, Y.H., et al., *Targeting Mitochondrial Metabolism as a Strategy to Treat Senescence.* Cells, 2021. **10**(11): p. 3003.
39. Chia, C.W., J.M. Egan, and L. Ferrucci, *Age-Related Changes in Glucose Metabolism, Hyperglycemia, and Cardiovascular Risk.* Circulation Research, 2018. **123**(7): p. 886-904.
40. Rosa, F.L.L., et al., *Aging Triggers Mitochondrial Dysfunction in Mice.* International Journal of Molecular Sciences, 2023. **24**(13): p. 10591.
41. Bou-Teen, D., et al., *Defective dimerization of FoF1-ATP synthase secondary to glycation favors mitochondrial energy deficiency in cardiomyocytes during aging.* Aging Cell, 2022. **21**(3).
42. Busch, K.B., *Inner mitochondrial membrane compartmentalization: Dynamics across scales.* The International Journal of Biochemistry & Cell Biology, 2020. **120**: p. 105694.
43. Cullis, P.R., M.J. Hope, and C.P.S. Tilcock, *Lipid Polymorphism and the roles of lipids in membranes.* Chemistry and Physics of Lipids, 1986. **40**: p. 127-144.
44. Gasanoff, E.S., L.S. Yaguzhinsky, and G. Garab, *Cardiolipin, Non-Bilayer Structures and Mitochondrial Bioenergetics: Relevance to Cardiovascular Disease.* Cells, 2021. **10**(7): p. 1721.

45. Lee, H.-J., et al., *Selective remodeling of cardiolipin fatty acids in the aged rat heart.* Lipids in Health and Disease, 2006. **5**(1).
46. Houtkooper, R.H. and F.M. Vaz, *Cardiolipin, the heart of mitochondrial metabolism.* Cellular and Molecular Life Sciences, 2008. **65**(16): p. 2493-2506.
47. Mileykovskaya, E. and W. Dowhan, *Cardiolipin-dependent formation of mitochondrial respiratory supercomplexes.* Chemistry and Physics of Lipids, 2014. **179**: p. 42-48.